

Analytic models of plausible gravitational lens potentials

Edward A. Baltz¹, Phil Marshall^{1,2}, Masamune Oguri¹

¹ Kavli Institute for Particle Astrophysics and Cosmology, Stanford University PO Box 20450, MS29, Stanford, CA 94309, USA

² Physics Department, University of California, Santa Barbara, CA 93601, USA

E-mail: eabaltz@slac.stanford.edu

Abstract.

Gravitational lenses on galaxy scales are plausibly modelled as having ellipsoidal symmetry and a universal dark matter density profile, with a Sersic profile to describe the distribution of baryonic matter. Predicting all lensing effects requires knowledge of the total lens potential: in this work we give analytic forms for that of the above hybrid model. Emphasising that complex lens potentials can be constructed from simpler components in linear combination, we provide a recipe for attaining elliptical symmetry in either projected mass or lens potential. We also provide analytic formulae for the lens potentials of Sersic profiles for integer and half-integer index. We then present formulae describing the gravitational lensing effects due to smoothly-truncated universal density profiles in cold dark matter model. For our isolated haloes the density profile falls off as radius to the minus fifth or seventh power beyond the tidal radius, functional forms that allow all orders of lens potential derivatives to be calculated analytically, while ensuring a non-divergent total mass. We show how the observables predicted by this profile differ from that of the original infinite-mass NFW profile. Expressions for the gravitational flexion are highlighted. We show how decreasing the tidal radius allows stripped haloes to be modelled, providing a framework for a fuller investigation of dark matter substructure in galaxies and clusters. Finally we remark on the need for finite mass halo profiles when doing cosmological ray-tracing simulations, and the need for readily-calculable higher order derivatives of the lens potential when studying catastrophes in strong lenses.

1. Introduction

A large number of cold dark matter (CDM) N-body simulations agree that the haloes formed have, on average, a universal broken power law density profile. While there is some debate over the logarithmic slope of the profile within the break, or scale radius r_s , and there is some scatter between haloes, it seems that the original profile of [1] (NFW) still provides a reasonable fit to the simulation data. This profile seems to be a generic feature of haloes formed in the hierarchical model of structure formation.

A number of authors have made significant progress in understanding non-linear effects in structure formation using halo models, where the number density, correlation function and mass density profile of CDM haloes are fitted to the numerical simulations and then used in a simplified model of large scale structure [2, 3, 4]. The NFW profile has played a prominent role in this enterprise. One application of the halo model is in the investigation of the halo occupation distribution, that characterises the substructure within a larger halo. This has long been one of the more controversial topics in CDM theory, with predictions and observations often at odds. In order to build up an accurate picture of a hierarchical mass distribution, the stripping of the sub-haloes by tidal gravitational forces must be modelled [5, 6]; measurements of halo stripping form an important test of the detailed predictions of the CDM simulations [7, 8].

Moreover, it is now clear that the effect of baryons on the shapes and profiles of total mass distributions cannot be ignored. In galaxies, the stellar component of the mass dominates at small radii giving rise to a peakier observed total density profile than seen in pure dark matter simulations [9]. The surface brightness profiles of massive galaxies seem to be consistently well-fitted by a Sersic profile of index 3 – 4 [10]; a logarithmic slope of -2 in total density in the inner regions appears ubiquitous [11]. Moreover, the dark matter profile itself is expected to steepen during the formation of the galaxy, by the process of adiabatic contraction [12, 13]. Typically this leads to more centrally concentrated, rounder haloes [14, 15]. The details of the mass distributions of real galaxies are therefore a probe of the galaxy formation physics claimed by the simulations.

Gravitational lensing allows us to probe the mass distributions of galaxies, groups and clusters in a unique way. Insensitive to the dynamical state of the lens system, both weak and strong lensing effects depend only on the projected (and scaled) gravitational potential. Gravitational lensing has already been used to investigate the density profile in galaxy clusters [16, 17, 18, 19]. Substructure studies have also been undertaken, making use of the galaxy-galaxy lensing effect in clusters [20]. The galaxy scale halo mass profiles have also been measured, using both strong lensing [21, 22, 9] and, in a more statistical fashion, galaxy-galaxy weak lensing [23, 24].

Lensing studies provide direct tests of the CDM simulations, and typically involve (at some point) fitting the parameters of an NFW-like model to the data. However, this model is also well-suited to a more general analysis, building up a data model from a linear combination of NFW-like potentials [25]. This approach has applications in

substructure characterisation, and also template-based cluster finding. Characterising stripped substructure both require an accurate treatment of the outer regions of haloes. However, in order to measure accurately density profile slopes and concentrations, the baryonic mass component must be included.

In the perpetually applicable thin lens approximation it is the projected Newtonian gravitational potential that gives rise to the gravitational lensing observables. Making the simplifying assumption that projected stellar mass density is proportional to optical surface brightness leads us to seek the potential that corresponds to the Sersic density profile. Likewise, for the dark matter component we require a lens potential that corresponds to the universal profile seen in simulations, but that also includes the effects of tidal stripping.

Analytic lens potentials are convenient to work with: they, and their derivatives that are needed for lensing data modelling, can be computed quickly and accurately; the introduction of ellipticity to the halo can be done very straightforwardly; more complex potentials can be constructed by simple linear combination of analytic functions. This last feature allows concave isodensity contours to be avoided in the case of high ellipticity. It also allows total density distributions to be constructed from mixtures of dark and luminous matter.

In this work we present analytic forms for a smoothly truncated universal CDM gravitational potential, and also for the potentials corresponding to a subset of the Sersic profiles. If the underlying potential is analytic, so are all the derivatives needed in gravitational lens studies. An outline of the paper is as follows. In Sections 2 and 3 we present our suggested analytic potential models, for both dark and baryonic matter components, and outline the derivation of the quantities relevant to gravitational lensing. We leave the full formulae to an appendix, but in Section 4 we plot the predicted observables, and compare them to those from an unstripped baryon-free NFW form. In Section 5 we briefly discuss our results, and point the reader towards some publically available computer code.

2. Smoothly truncated dark matter haloes

The NFW profile for the CDM density ρ of a halo is

$$\rho(r) = \frac{4\delta_c\rho_{\text{crit}}}{\left(\frac{r}{r_s}\right)\left(1 + \frac{r}{r_s}\right)^2} = \frac{M_0}{4\pi r(r+r_s)^2}. \quad (1)$$

The characteristic overdensity δ_c is the density at the scale radius r_s , in units of the critical density ρ_{crit} . Alternatively, we can express this as $\rho(r_s) = \delta_c\rho_{\text{crit}} = M_0/(16\pi r_s^3)$. The NFW profile is analytically integrable along the line of sight; the most frequently used formulae for the weak lensing shear [26] and strong lensing image positions [27] were derived assuming the integral to extend over all space. Given that the NFW profile has divergent total mass, [4] suggest using a modified form that is sharply truncated at the

virial radius. The projection integral is then more realistic, with only mass physically associated with a finite-sized halo being modelled.

We might expect real CDM haloes to be truncated due to tidal effects; a step-function density cutoff may not offer a very physical picture of the edges of haloes. With the [4] mass distribution, the lensing deflection angle and shear are tractable (if somewhat less simple), and the actual potential is worse still, involving (at least) polylogarithms. Also, the convergence and shear are not differentiable at the truncation radius. A power-law cutoff in the potential is more attractive in this regard. We should insist that the truncated profile match that of NFW as closely as possible within the tidal radius, which is introduced as the third parameter of the profile. This is important for the results from previous work on fitting the outputs from N-body simulations pertaining not only to the density profile but also the mass function [28].

With these desiderata in mind, we suggest the following functional form for a smoothly truncated universal 3-d mass density profile:

$$\rho(r) = \frac{4\delta_c \rho_{\text{crit}}}{\left(\frac{r}{r_s}\right) \left(1 + \frac{r}{r_s}\right)^2 \left(1 + \left(\frac{r}{r_t}\right)^2\right)^n} = \frac{M_0}{4\pi r(r+r_s)^2} \left(\frac{r_t^2}{r^2 + r_t^2}\right)^n. \quad (2)$$

Here, r_t is a new parameter which should correspond to the tidal radius for tidally truncated halos [29]. The parameter n controls the sharpness of the truncation; we will investigate the cases $n = 1, 2$. For relatively isolated haloes, we expect the tidal radius to be much larger than the scale radius. We define $\tau = r_t/r_s$, expecting $\tau \gg 1$. Note that τ is not necessarily the ‘‘concentration’’ parameter, defined as the ratio of a ‘‘virial’’ radius to r_s . In the left-hand panel of Figure 1, we plot this profile in the usual way (with logarithmic axes), and compare with the original NFW profile. We show the effect of the tidal radius in providing a smooth edge to the halo. In the right-hand panel of Figure 1 we show the integrated projected mass profile, for the same set of density profiles. In this panel radius is projected radius, and the logarithmic divergence of the original NFW profile can be clearly seen. Projected mass within some appropriate radius is (approximately) the quantity that is best constrained by gravitational lensing – in Section 4 we show the predicted observables of gravitational lensing in more detail.

After some experimentation we found that the form recommended above is indeed the simplest one that gives an analytic potential while ensuring a non-diverging total mass for all values of the tidal radius. In the case where the tidal radius r_t is outside the scale radius r_s , the $n = 1$ profile falls off as r^{-5} , steep enough to mimic a sharp cutoff. If the tidal radius were to lie inside the scale radius, then the density would decrease as r^{-3} initially before turning over to r^{-5} outside r_s . Since this would imply some memory of the original halo after the presumably violent act of tidal stripping, we suggest that if $r_t < r_s$, the $n = 2$ version of the density profile be used. For $r_t < r_s$, this profile turns over to r^{-5} at r_t , which is effectively a sharp cutoff. The further turnover to r^{-7} at $r_s > r_t$ has little effect.

The close agreement of the unstripped halo with the original NFW profile is comforting. For example, for a halo with a concentration of 10, if we set r_t to twice

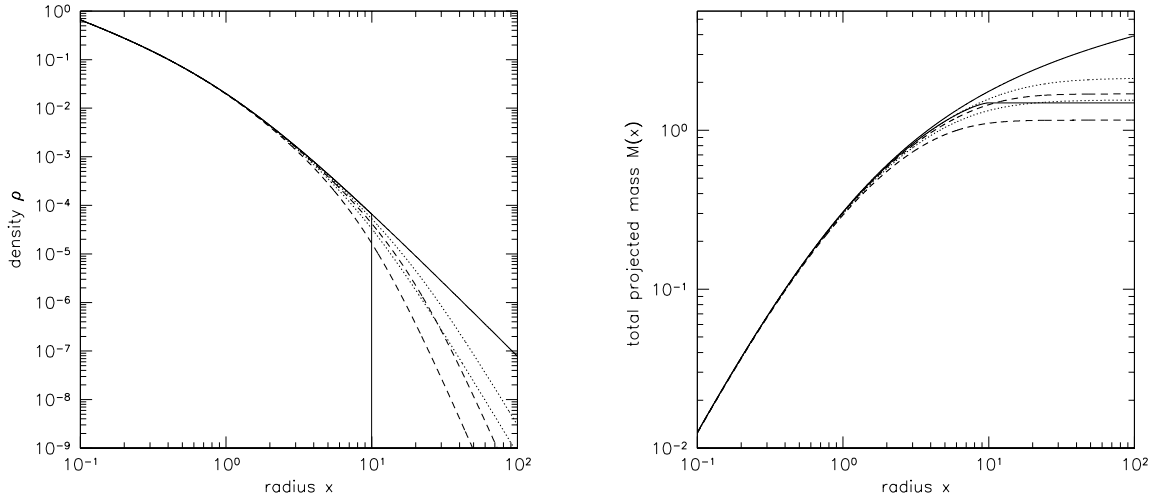


Figure 1. Density (left) and integrated projected mass (right) profiles for NFW haloes with various truncation schemes. The solid lines indicate the original NFW halo, with and without a hard cutoff at $\tau = r_t/r_s = 10$. Dotted lines show the $n = 1$ cutoff prescription, with $\tau = 10, 20$. Dashed lines show the $n = 2$ cutoff prescription, again with $\tau = 10, 20$. For smoothly truncated models, ratios of masses outside the virial radius to the virial mass, $[M_{\text{tot}} - M(< 10)]/M(< 10)$, are 17% for $(n, \tau) = (1, 10)$, 4.6% for $(2, 10)$, 36% for $(1, 20)$, and 17% for $(2, 20)$. Note that this ratio is infinity for the original NFW halo because it has divergent total mass.

the virial radius ($\tau = 20$), the masses contained within the virial radius are the same to within 6%. Of course the total mass of the truncated halo is 50% larger than the virial mass, while the total mass of the untruncated halo (formally) diverges. We will thus take $r_t = 2r_{200}$ as our fiducial tidal radius for an unstripped halo. We note that this choice of the truncation radius is simply a working assumption in this paper, and the more appropriate value should eventually be obtained in N -body simulations and observations.

3. Lensing by stellar mass in galaxies

The Sersic profile, found to fit well the optical surface brightness I of undisturbed galaxies [30], is

$$I(r) = I_e \exp \left[\kappa_n \left(1 - \frac{r}{r_e} \right)^{1/n} \right], \quad (3)$$

where the effective radius r_e is the radius within which half the flux is contained, and n is the Sersic index. For elliptical galaxies, an index of around 4 is often seen [31], while the characteristic exponential profile of galaxy disks corresponds to a Sersic index of 1. In fact, a broad range of Sersic index values have been seen in fits to observed galaxy light profiles [32]. In addition, there has been some arguments that density profiles of CDM haloes can also be fitted well by the Sersic profile with an index of 2 – 3. [33, 34].

Assuming that stellar mass follows light, we can substitute surface mass density Σ for surface brightness in equation 3. In the appendix, we show that the lens potential sourced by this mass distribution [35] is analytically tractable for integer and half-integer n .

4. Predicted observables

As we show in the appendix, both density profiles introduced above (truncated NFW and Sersic) have analytic lens potentials. (The NFW profile has an analytic three-dimensional potential, which can itself be projected analytically.) The expressions for the lensing potential, while somewhat lengthy, are rapidly calculated and differentiable to all orders. In this section we plot some of these derivatives, pointing out their application in gravitational lens data modelling. We note that in the limit of radii beyond the tidal radius the lensing properties of our model haloes do indeed approach those of a point mass, as required.

4.1. Weak lensing

We first address the issue of not truncating the NFW profile on the weak lensing shear and convergence (see [36] for a good introduction to these quantities). The lefthand panel of Figure 2 shows the convergence (projected mass density) profile for the set of haloes first introduced in Figure 1.

We see that using a truncated profile with the same virial mass somewhat reduces the predicted lensing effect. The corresponding shear profiles are plotted in the right-hand panel of Figure 2. Taking the central density profiles to be equal (mimicking a well-constrained central strong lensing region, for example), for $\tau = 20$ we note that the virial mass (mass within $10r_s$) is 6% less for the $n = 1$ truncated halo. The shear for the two profiles only differs by 3%, however. The total *projected* mass within the projected virial radius is some 12% lower than that of the untruncated profile. Lastly, the surface density of the truncated halo is 30% lower at $10r_s$.

The difference in reduced shear $\gamma/|1 - \kappa|$ thus depends on the absolute value of the convergence, relative to the critical surface density, but can be significant. Very roughly, from Figure 2 we expect that different truncations examined in this paper can yield $\sim 10\%$ difference in γ at around the virial radius. Although this is smaller than the accuracy of shear measurements for most massive clusters of galaxies (e.g., [37]), the accuracy can be reachable in the weak lensing analysis of stacked cluster samples (e.g., [38]).

4.2. Strong and intermediate lensing

Figure 3 shows the amplitude of the deflection angle for a strongly lensed source. Here we see that using a truncated profile has very little effect on the deflection angle in the regime where it is measurable as a multiple-image separation ($r < r_s$). This is

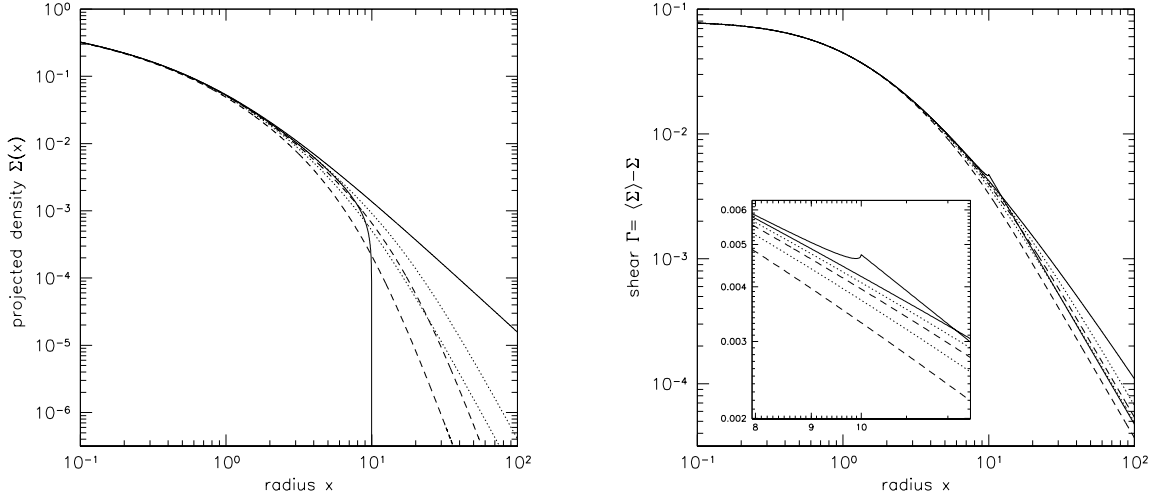


Figure 2. Convergence (left) and shear (right) for NFW haloes. The curve line styles are the same as in Figure 1. Projected mass density Σ (directly proportional to convergence κ) is plotted on the left, showing that a hard cutoff in density results in a softer, but still non-differentiable, cutoff in the convergence. Actually plotted on the right is $\langle \Sigma \rangle - \Sigma$, which is directly proportional to the shear γ for axisymmetric haloes. Notice that a hard cutoff in density means the shear is finite, but not differentiable at the cutoff radius.

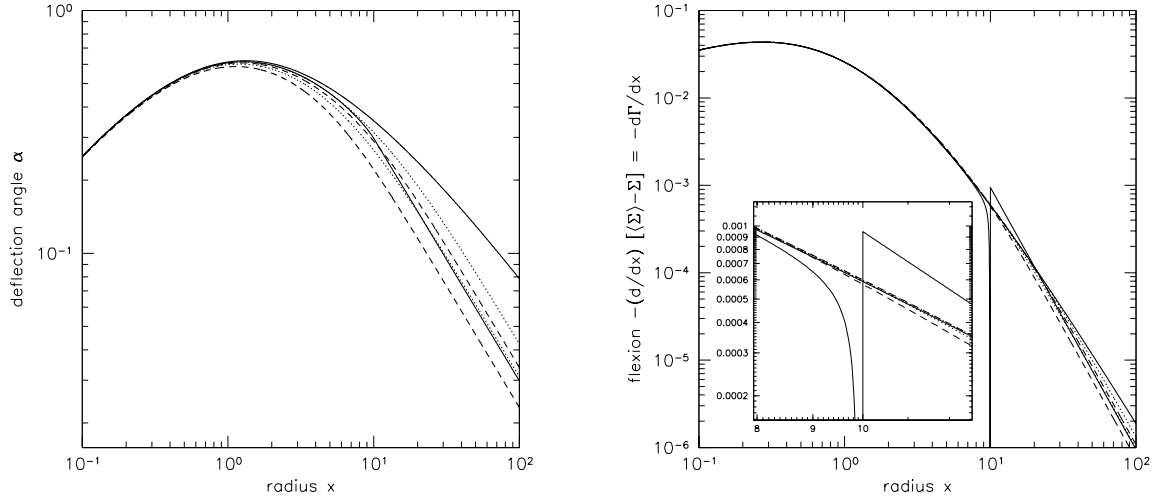


Figure 3. Deflection angle (left) and flexion (right) for NFW haloes. Curves are the same as in Figure 1. Notice that the hard cutoff in density causes the flexion to diverge at the cutoff radius. As the flexion approaches $-\infty$, so it changes sign as well. This can be seen in Figure 2, where the shear actually starts to increase as the cutoff radius is approached.

unsurprising given that the strong lensing is dominated by the central part of the profile which is, by design, little changed in our new model.

In contrast, the so-called “flexion” may be more strongly affected by the truncation

because it is essentially the higher-order derivative of the lens potential. In addition it is measurable over a wide range of scales from the Einstein radius to (in a statistical sense) the virial radius. In Figure 3 we plot the third derivative of the lens potential: the most interesting component of flexion for circular symmetry is in fact just this, the radial gradient of the shear. Marked differences in signal strength arise when the haloes are truncated.

A plausible model for an elliptical galaxy lens consists of two parts: the stellar component and the dark halo. Modelling the stellar component as an $n = 4$ Sersic profile and the dark halo as a truncated NFW profile with concentration 10 and $\tau = 20$, a reasonable fit to lensing data can be made [39]. The salient feature is that the total mass profile is approximately isothermal. This can be arranged with the following prescription (for $\tau = 20$ and $n = 4$):

$$\frac{M_{\text{NFW}}}{M_{\text{deV}}} \approx 4.75 \frac{r_s}{r_e}. \quad (4)$$

The NFW mass is the total mass. The virial mass (mass within 10 scale radii in this case) is 0.66 of the total. The broad isothermal region obtained by this prescription is illustrated in Figure 4. We note that adiabatic contraction [12, 13, 14] modifies the NFW profile, leading to more centrally concentrated profile of dark matter. However, the effect of adiabatic contraction is most pronounced at the very center of the halo where the baryonic (Sersic) component is dominated, and thus its effect on the total mass profile is not substantial.

Finally we move to two dimensions and illustrate the construction of elliptically symmetric isophotes in the convergence distribution. It has been noted [40] that the isodensity contours of an elliptical lens potential can become dumbbell-shaped at low values of the axis ratio. In the appendix we show how isodensity contours that are elliptical to third order in the axis ratio can be constructed following a simple recipe. In Figure 5 we illustrate this procedure, showing the constituent concentric elliptical potentials and the resulting convergence contours. It is found that our new model not only avoids the unphysical concave isodensity but also gives much better fit to the elliptical isodensity than the elliptical lens potential. For large axis ratios (3:1 is as large as is feasible by our technique), the isodensity contours are slightly disk-like. We note that this recipe preserves the radial profile of the (self-similar) constituent potentials. Although the procedure is derived assuming a pure power-law, the nearly isothermal distribution of the composite model illustrated in Figure 4 suggests that our prescription is useful for such composite model, at least as long as the ellipticities of Sersic and NFW components are similar.

5. Discussion

We have introduced a simple smoothly-truncated extension of the NFW density profile. To date the majority of cluster and galaxy lens modelling that has been performed using the NFW profile has used the untruncated profile. We find that, if haloes are indeed

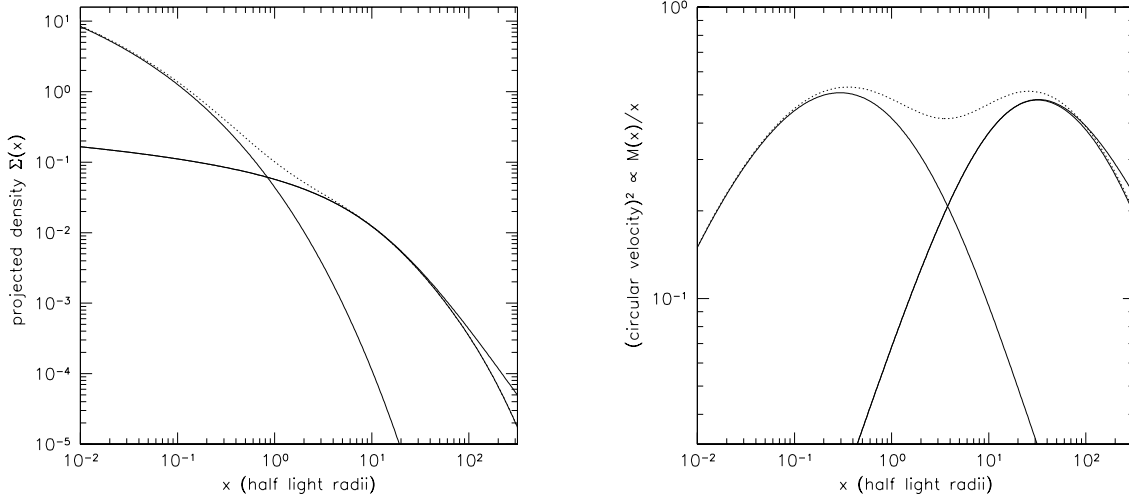


Figure 4. Sersic ($n=4$) profile combined with NFW profile. We plot the convergence (left) and circular velocity squared $M(x)/x$ (right) associated with each component (there are two curves for the NFW profile: one untruncated and one with $\tau = 20$), along with the total (dashed line). The truncated NFW profile is 70 times more massive than the Sersic profile (the virial mass is 50 times larger than the stellar mass), and the scale radius is 15 times larger than the half light radius. With these reasonable parameters, it is clear that the total profile is nearly isothermal (logarithmic slope of -1 in convergence) around the half light radius. In fact, we find that (for $\tau = 20$), the relation $M_{\text{NFW}}/M_{\text{deV}} = 4.75 r_s/r_e$ gives a flat region in velocity dispersion.

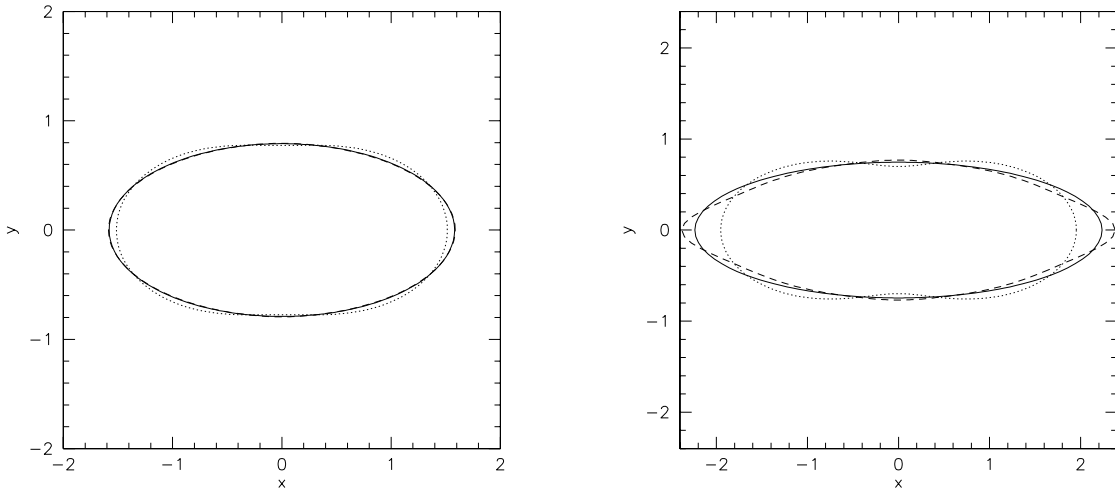


Figure 5. Convergence (isodensity) contours for three stacked elliptical potentials. True ellipses are shown as solid curves, three stacked potentials are shown as dashed curves, and single elliptical potentials are shown as dotted curves. The left panel illustrates the case $\epsilon_{\text{izo}} = 0.6$ (axis ratio 2:1), while the right panel illustrates $\epsilon_{\text{izo}} = 0.8$ (axis ratio 3:1). The slight diskiness of the isodensity contours can be seen especially for the $\epsilon_{\text{izo}} = 0.8$ case. The fitting procedure is described in Appendix C.

tidally-moulded leading to the kinds of smooth truncation that we propose, then the masses of the haloes may have been overestimated by some 10% or so during a weak lensing analysis. This number pertains to the situation where the inner profile is inferred to be the same for each model profile, as might be the case when good strong lensing data are available. We find that the smooth truncation of a halo does not significantly affect the deflection angles at the image positions (which lie typically well within the scale radius). If strong lensing data are not available then the degeneracy between the truncation radius and the halo mass will give rise to a broader inferred marginal probability distribution for the halo mass, with the mean shifting to lower values than for the untruncated profile.

The truncation of galaxy haloes in field galaxy-galaxy lensing is always likely to be masked by the effects of large scale structure on the outer parts of the mass profile (the “two-halo” term). However, in clusters a 10% systematic error is comparable to that introduced in other parts of a current weak (plus strong) lensing analysis. The uncertain background galaxy redshift distribution, additional mass along the line of sight, cluster member galaxy contamination, projection effects, and shear calibration errors can easily be of order 10% in the halo mass. However, as survey sizes increase, and the goals of cosmological cluster-counting experiments become loftier, uncertainties such as that introduced by halo truncation may become important.

Sharp truncation [4] introduces discontinuities in the shear that are unlikely to cause problems in data modelling; however, the same may not be true about flexion, where a singularity appears at the truncation radius. Smooth truncation (or indeed, no truncation) avoids this problem.

Galaxy-galaxy weak lensing studies within clusters of galaxies have already succeeded in producing a measurement of a truncation radius [41]. The combined Sersic plus NFW model currently popular in field galaxy lens modelling could profitably be applied in a cluster galaxy-galaxy lensing. The photometry provides extra constraints on the stellar mass part of the density profile [42], allowing the dark matter structure of galaxies in clusters to be probed. The model suggested here would straightforwardly allow strong and intermediate lensing effects to be incorporated; we are not far from possessing a useful sample of strong gravitational lenses lying in clusters.

The question of how best to model tidal-truncation of dark matter haloes has been approached here in a phenomenological and pragmatic way: we wanted an analytic form for the lens potential. We believe the forms presented here would provide good fits to the haloes seen in numerical simulations, based on the successes of others with very similar profiles [5, 22]. We have shown that plausible models of gravitational lenses can be constructed from the superposition of simple analytic profiles, including the generation of elliptically-symmetric isodensity contours. An interesting extension of this would be to attempt to build up still more complex mass distributions, from misaligned and offset building blocks [25]. Again, whether the haloes and sub-haloes observed in numerical simulations can be well-enough approximated by such a model remains to be seen. At present it seems that the signal-to-noise in Einstein rings is sufficiently high to constrain

such a more complex model [43, 9].

Finally, we discuss the importance of truncation, and a smooth one at that, in when simulating lensing effects in large surveys. Gravitational lensing, weak, intermediate and strong, may be expected to be an important component of multiple-pronged dark energy investigation. Simulations of large fields will play a vital role in improving our understanding of the astrophysical systematic errors present in cosmic shear, and cluster mass function, measurements. Halo models are a cheap and efficient way of doing this, capturing the pertinent physical effects without the need for further CPU-expensive N-body simulations. However, ray-tracing through halo models does present some technical challenges [4, 44]. The smooth analytic truncation proposed here allows the mass budget to be balanced, while allowing all gravitational lensing effects to be calculated rapidly to machine precision. In fact, it has been shown that the shear angular correlation function becomes $\sim 20\%$ smaller if the truncation at around the virial radius is included, and that the calculation with the truncation shows better agreement with N-body simulations [4].

A by-product of the future large optical and radio imaging surveys will be an interesting sample of strong lenses showing higher-order catastrophes beyond the usual cusps and folds. These systems provide very high magnifications, and are very sensitive to the mass structure in the lens, and as such promise to be interesting laboratories. However, modelling them will require an accurate multi-scale approach; we leave the development of this project to further work.

The code used in this work is plain ISO C99 and can be freely downloaded from

<http://kipac.stanford.edu/collab/research/lensing/ample/>

Acknowledgments

We thank James Taylor, Peter Schneider, Stelios Kazantzidis, and Masahiro Takada for useful discussions and encouragement. We also thank an anonymous referee for many suggestions. This work was supported in part by the U.S. Department of Energy under contract number DE-AC02-76SF00515. PJM acknowledges support from the TABASGO foundation in the form of a research fellowship.

References

- [1] J.F. Navarro, C.S. Frenk, and S.D.M. White. *ApJ*, 490:493, 1997.
- [2] H. J. Mo and S. D. M. White. An analytic model for the spatial clustering of dark matter haloes. *Mon. Not. Roy. Astro. Soc.*, 282:347–361, September 1996.
- [3] A. Cooray, W. Hu, and J. Miralda-Escudé. Weak Lensing by Large-Scale Structure: A Dark Matter Halo Approach. *Astrophys. J.*, 535:L9–L12, May 2000.

- [4] M. Takada and B. Jain. The three-point correlation function in cosmology. *Mon. Not. Roy. Astro. Soc.*, 340:580–608, April 2003.
- [5] J. E. Taylor and A. Babul. The evolution of substructure in galaxy, group and cluster haloes - I. Basic dynamics. *Mon. Not. Roy. Astro. Soc.*, 348:811–830, March 2004.
- [6] M. Oguri and J. Lee. A realistic model for spatial and mass distributions of dark halo substructures: An analytic approach. *Mon. Not. Roy. Astro. Soc.*, 355:120–128, November 2004.
- [7] E. Hayashi, J. F. Navarro, J. E. Taylor, J. Stadel, and T. Quinn. The Structural Evolution of Substructure. *Astrophys. J.*, 584:541–558, February 2003.
- [8] J. E. Taylor and A. Babul. The evolution of substructure in galaxy, group and cluster haloes - III. Comparison with simulations. *Mon. Not. Roy. Astro. Soc.*, 364:535–551, December 2005.
- [9] L. V. E. Koopmans, T. Treu, A. S. Bolton, S. Burles, and L. A. Moustakas. The Sloan Lens ACS Survey. III. The Structure and Formation of Early-Type Galaxies and Their Evolution since $z \sim 1$. *Astrophys. J.*, 649:599–615, October 2006.
- [10] I. Trujillo, P. Erwin, A. Asensio Ramos, and A. W. Graham. Evidence for a New Elliptical-Galaxy Paradigm: Sérsic and Core Galaxies. *Astron. J.*, 127:1917–1942, April 2004.
- [11] T. Treu, L. V. Koopmans, A. S. Bolton, S. Burles, and L. A. Moustakas. The Sloan Lens ACS Survey. II. Stellar Populations and Internal Structure of Early-Type Lens Galaxies. *Astrophys. J.*, 640:662–672, April 2006.
- [12] Y. B. Zeldovich, A. A. Klypin, M. Y. Khlopov, and V. M. Chechetkin. *Soviet J. Nucl. Phys.*, 31:664, 1980.
- [13] G. R. Blumenthal, S. M. Faber, R. Flores, and J. R. Primack. Contraction of dark matter galactic halos due to baryonic infall. *Astrophys. J.*, 301:27–34, February 1986.
- [14] O. Y. Gnedin, A. V. Kravtsov, A. A. Klypin, and D. Nagai. Response of Dark Matter Halos to Condensation of Baryons: Cosmological Simulations and Improved Adiabatic Contraction Model. *Astrophys. J.*, 616:16–26, November 2004.
- [15] S. Kazantzidis, A. V. Kravtsov, A. R. Zentner, B. Allgood, D. Nagai, and B. Moore. The Effect of Gas Cooling on the Shapes of Dark Matter Halos. *Astrophys. J.*, 611:L73–L76, August 2004.
- [16] J. Kneib, P. Hudelot, R. S. Ellis, T. Treu, G. P. Smith, P. Marshall, O. Czoske, I. Smail, and P. Natarajan. A Wide-Field Hubble Space Telescope Study of the Cluster Cl 0024+1654 at $z=0.4$. II. The Cluster Mass Distribution. *ApJ*, 598:804–817, December 2003.
- [17] R. Gavazzi, B. Fort, Y. Mellier, R. Pelló, and M. Dantel-Fort. A radial mass profile analysis of the lensing cluster MS 2137.3-2353. *A&A*, 403:11–27, May 2003.

- [18] D. J. Sand, T. Treu, G. P. Smith, and R. S. Ellis. The Dark Matter Distribution in the Central Regions of Galaxy Clusters: Implications for Cold Dark Matter. *ApJ*, 604:88–107, March 2004.
- [19] T. Broadhurst, M. Takada, K. Umetsu, X. Kong, N. Arimoto, M. Chiba, and T. Futamase. The Surprisingly Steep Mass Profile of A1689, from a Lensing Analysis of Subaru Images. *ApJL*, 619:L143–L146, February 2005.
- [20] P. Natarajan and V. Springel. Abundance of Substructure in Clusters of Galaxies. *ApJL*, 617:L13–L16, December 2004.
- [21] D. Rusin, C. S. Kochanek, and C. R. Keeton. Self-similar Models for the Mass Profiles of Early-Type Lens Galaxies. *ApJ*, 595:29–42, September 2003.
- [22] S. Dye and S. J. Warren. Decomposition of the Visible and Dark Matter in the Einstein Ring 0047-2808 by Semilinear Inversion. *Astrophys. J.*, 623:31–41, April 2005.
- [23] E. S. Sheldon, D. E. Johnston, J. A. Frieman, R. Scranton, T. A. McKay, A. J. Connolly, T. Budavári, I. Zehavi, N. A. Bahcall, J. Brinkmann, and M. Fukugita. The Galaxy-Mass Correlation Function Measured from Weak Lensing in the Sloan Digital Sky Survey. *AJ*, 127:2544–2564, May 2004.
- [24] H. Hoekstra, H. K. C. Yee, and M. D. Gladders. Properties of Galaxy Dark Matter Halos from Weak Lensing. *ApJ*, 606:67–77, May 2004.
- [25] P. Marshall. Physical component analysis of galaxy cluster weak gravitational lensing data. *Mon. Not. Roy. Astro. Soc.*, 372:1289–1298, November 2006.
- [26] C. O. Wright and T. G. Brainerd. Gravitational Lensing by NFW Halos. *ApJ*, 534:34–40, May 2000.
- [27] M. Bartelmann. Arcs from a universal dark-matter halo profile. *A&A*, 313:697, 1996.
- [28] A. Jenkins, C. S. Frenk, S. D. M. White, J. M. Colberg, S. Cole, A. E. Evrard, H. M. P. Couchman, and N. Yoshida. The mass function of dark matter haloes. *MNRAS*, 321:372–384, 2001.
- [29] J. Binney and S. Tremaine. *Galactic dynamics*. Princeton, NJ, Princeton University Press, 1987, 747 p., 1987.
- [30] J. L. Sersic. *Atlas de Galaxias Australes*. Cordoba: Obs. Astron., Univ. Nac. Cordoba, 1968.
- [31] G. de Vaucouleurs. *Ann. d’Astrophys.*, 11:247, 1948.
- [32] M. R. Blanton, D. Eisenstein, D. W. Hogg, D. J. Schlegel, and J. Brinkmann. Relationship between Environment and the Broadband Optical Properties of Galaxies in the Sloan Digital Sky Survey. *Astrophys. J.*, 629:143–157, August 2005.
- [33] D. Merritt, J. F. Navarro, A. Ludlow, and A. Jenkins. A Universal Density Profile for Dark and Luminous Matter? *Astrophys. J.*, 624:L85–L88, May 2005.

- [34] B. Terzić and A. W. Graham. Density-potential pairs for spherical stellar systems with Sérsic light profiles and (optional) power-law cores. *Mon. Not. Roy. Astro. Soc.*, 362:197–212, September 2005.
- [35] V. F. Cardone. The lensing properties of the Sersic model. *Astron. Astrophys.*, 415:839–848, March 2004.
- [36] P. Schneider. Weak Gravitational Lensing. In G. Meylan, P. Jetzer, and P. North, editors, *Gravitational Lensing: Strong, Weak & Micro*, Lecture Notes of the 33rd Saas-Fee Advanced Course. Springer-Verlag: Berlin, 2006.
- [37] T. Broadhurst, K. Umetsu, E. Medezinski, M. Oguri, and Y. Rephaeli. Comparison of Cluster Lensing Profiles with Λ CDM Predictions. *Astrophys. J.*, 685:L9–L12, September 2008.
- [38] D. E. Johnston, E. S. Sheldon, R. H. Wechsler, E. Rozo, B. P. Koester, J. A. Frieman, T. A. McKay, A. E. Evrard, M. R. Becker, and J. Annis. Cross-correlation Weak Lensing of SDSS galaxy Clusters II: Cluster Density Profiles and the Mass–Richness Relation. *ArXiv e-prints*, September 2007.
- [39] R. Gavazzi, T. Treu, J. D. Rhodes, L. V. E. Koopmans, A. S. Bolton, S. Burles, R. J. Massey, and L. A. Moustakas. The Sloan Lens ACS Survey. IV. The Mass Density Profile of Early-Type Galaxies out to 100 Effective Radii. *Astrophys. J.*, 667:176–190, September 2007.
- [40] A. Kassiola and I. Kovner. Elliptic Mass Distributions versus Elliptic Potentials in Gravitational Lenses. *Astrophys. J.*, 417:450–+, November 1993.
- [41] P. Natarajan, J.-P. Kneib, and I. Smail. Evidence for Tidal Stripping of Dark Matter Halos in Massive Cluster Lenses. *Astrophys. J.*, 580:L11–L15, November 2002.
- [42] P. Natarajan and J.-P. Kneib. Lensing by galaxy haloes in clusters of galaxies. *Mon. Not. Roy. Astro. Soc.*, 287:833–847, June 1997.
- [43] L. V. E. Koopmans. Gravitational imaging of cold dark matter substructures. *Mon. Not. Roy. Astro. Soc.*, 363:1136–1144, November 2005.
- [44] M. Oguri. The image separation distribution of strong lenses: halo versus subhalo populations. *Mon. Not. Roy. Astro. Soc.*, 367:1241–1250, April 2006.
- [45] D. M. Goldberg and D. J. Bacon. Galaxy-Galaxy Flexion: Weak Lensing to Second Order. *Astrophys. J.*, 619:741–748, February 2005.
- [46] D. J. Bacon, D. M. Goldberg, B. T. P. Rowe, and A. N. Taylor. Weak gravitational flexion. *Mon. Not. Roy. Astro. Soc.*, 365:414–428, January 2006.

Appendix A. Truncated NFW Profile

The Navarro, Frenk and White (NFW) profile is given by

$$\rho(r) = \frac{M_0}{4\pi} \frac{1}{r(r+r_s)^2}. \quad (\text{A.1})$$

Defining $x = r/r_s$,

$$\rho(x) = \frac{M_0}{4\pi r_s^3} \frac{1}{x(1+x)^2}. \quad (\text{A.2})$$

This profile describes dark matter haloes well, out to the virial radius. However it suffers from the deficiency that it has infinite mass. The truncation radius is defined to be a factor of τ larger than the scale radius. With the sole motivation of allowing “simple” analytic forms, we propose the following truncated NFW profile:

$$\rho_T(x) = \frac{M_0}{4\pi r_s^3} \frac{1}{x(1+x)^2} \frac{\tau^2}{\tau^2 + x^2}. \quad (\text{A.3})$$

This form is quite similar to the NFW profile for $x < \tau$, i.e. inside the truncation radius. Furthermore, the total mass is finite,

$$M = M_0 \frac{\tau^2}{(\tau^2 + 1)^2} [(\tau^2 - 1) \ln \tau + \tau\pi - (\tau^2 + 1)]. \quad (\text{A.4})$$

In the limit $\tau \rightarrow \infty$, we recover the logarithmically divergent mass of the NFW profile.

For purposes of gravitational lensing, we are interested in the projected mass density. We first define the function

$$F(x) = \frac{\cos^{-1}(1/x)}{\sqrt{x^2 - 1}}. \quad (\text{A.5})$$

This function is well defined everywhere: taking the appropriate limit $F(1) = 1$, and for $x < 1$, where both the numerator and denominator are purely imaginary, we choose the branch where $F(x) > 0$. Note that `ArcCos` from Mathematica and `cacos` from C99 disagree on the sign of $\cos^{-1}(x)$ when $x > 1$. Note that in the $x \rightarrow 0$ limit it reduces to $F(x) = \ln(2/x)$. We also define the following logarithm, which will appear many times,

$$L(x) = \ln \left(\frac{x}{\sqrt{\tau^2 + x^2} + \tau} \right). \quad (\text{A.6})$$

With these definitions, the projected surface mass density is given by

$$\Sigma(x) = r_s \int_{-\infty}^{\infty} d\ell \rho_T(\sqrt{\ell^2 + x^2}) \quad (\text{A.7})$$

$$= \frac{M_0}{r_s^2} \frac{\tau^2}{2\pi(\tau^2 + 1)^2} \left\{ \frac{\tau^2 + 1}{x^2 - 1} [1 - F(x)] + 2F(x) - \frac{\pi}{\sqrt{\tau^2 + x^2}} + \frac{\tau^2 - 1}{\tau\sqrt{\tau^2 + x^2}} L(x) \right\}. \quad (\text{A.8})$$

Notice that for $x \rightarrow 1$, the first term requires that a limit be taken. As before, in the $\tau \rightarrow \infty$ limit we recover the result for the NFW profile,

$$\Sigma(x) = \frac{M_0}{r_s^2} \frac{1 - F(x)}{2\pi(x^2 - 1)} + O\left(\frac{\ln \tau}{\tau^2}\right). \quad (\text{A.9})$$

We can derive the convergence κ simply by taking $\kappa = \Sigma/\Sigma_{\text{crit}}$. We will also need the total projected mass inside radius x ,

$$M_{\text{proj}}(x) = r_s^2 \int_0^x dx' 2\pi x' \Sigma(x') \quad (\text{A.10})$$

$$= M_0 \frac{\tau^2}{(\tau^2 + 1)^2} \left\{ [\tau^2 + 1 + 2(x^2 - 1)] F(x) + \tau\pi + (\tau^2 - 1) \ln \tau + \sqrt{\tau^2 + x^2} \left[-\pi + \frac{\tau^2 - 1}{\tau} L(x) \right] \right\}. \quad (\text{A.11})$$

We again recover the NFW result in the $\tau \rightarrow \infty$ limit,

$$M_{\text{proj}}(x) = M_0 \left(F(x) + \ln \frac{x}{2} \right) + O\left(\frac{\ln \tau}{\tau^2}\right). \quad (\text{A.12})$$

A crucial quantity is the shear of the gravitational field. The simplest way to derive it for a circularly symmetric lens is to use the mean projected surface density inside radius x , which is simply $\bar{\Sigma} = M_{\text{proj}}/\pi r^2$. Defining $\Gamma = \bar{\Sigma} - \Sigma$, the shear is then $\gamma = \Gamma/\Sigma_{\text{crit}}$.

We can now derive the lensing potential. Including the famous factor of two, and defining $u = x^2$,

$$\psi(u) = \frac{4G}{c^2} \int_0^{\sqrt{u}} \frac{dx'}{x'} M_{\text{proj}}(x') = \frac{2G}{c^2} \int_0^u \frac{du'}{u'} M_{\text{proj}}(\sqrt{u'}). \quad (\text{A.13})$$

The potential is thus

$$\begin{aligned} \psi(u) = \frac{2GM_0}{c^2} \frac{1}{(\tau^2 + 1)^2} & \left\{ 2\tau^2\pi \left[\tau - \sqrt{\tau^2 + u} + \tau \ln \left(\tau + \sqrt{\tau^2 + u} \right) \right] \right. \\ & + 2(\tau^2 - 1)\tau\sqrt{\tau^2 + u} L(\sqrt{u}) + \tau^2(\tau^2 - 1) L^2(\sqrt{u}) \\ & + 4\tau^2(u - 1)F(\sqrt{u}) + \tau^2(\tau^2 - 1) \left(\cos^{-1} \frac{1}{\sqrt{u}} \right)^2 \\ & + \tau^2 [(\tau^2 - 1) \ln \tau - \tau^2 - 1] \ln u \\ & \left. - \tau^2 [(\tau^2 - 1) \ln \tau \ln(4\tau) + 2 \ln(\tau/2) - 2\tau(\tau - \pi) \ln(2\tau)] \right\} \end{aligned} \quad (\text{A.14})$$

The resulting potential has the correct behavior in the $\tau \rightarrow \infty$ limit for all values of u ,

$$\psi(u) = \frac{2GM_0}{c^2} \left[\left(\cos^{-1} \frac{1}{\sqrt{u}} \right)^2 + \ln^2 \left(\frac{\sqrt{u}}{2} \right) \right] + O\left(\frac{\ln \tau}{\tau^2}\right). \quad (\text{A.15})$$

We also verify that for $u \gg \tau$, the potential is that of a point mass of the correct total mass (up to an irrelevant constant A),

$$\begin{aligned} \psi(u) = A + \frac{4GM_0}{c^2} \frac{\tau^2}{(\tau^2 + 1)^2} & [(\tau^2 - 1) \ln \tau + \tau\pi - (\tau^2 + 1)] \ln \sqrt{u} \\ & + O\left(\frac{\tau^2}{u}\right) \end{aligned} \quad (\text{A.16})$$

$$= A + \frac{4GM}{c^2} \ln \sqrt{u} + O\left(\frac{\tau^2}{u}\right). \quad (\text{A.17})$$

We can now calculate the derivatives of ψ . The first is obvious,

$$\psi'(u) = \frac{2G}{c^2} \frac{M_{\text{proj}}(\sqrt{u})}{u}. \quad (\text{A.18})$$

Next is slightly messier,

$$\psi''(u) = \frac{2G}{c^2} \left[-\frac{M_{\text{proj}}(\sqrt{u})}{u^2} + \frac{\pi r_s^2 \Sigma(\sqrt{u})}{u} \right] = -\frac{2\pi G r_s^2 \Gamma}{c^2 u} \quad (\text{A.19})$$

$$\begin{aligned} &= \frac{2GM_0}{c^2} \frac{\tau^2}{2(\tau^2 + 1)^2 u^2} \left[2(1 - u - \tau^2) F(\sqrt{u}) - 2(\tau^2 - 1) \ln \tau \right. \\ &\quad - \frac{(\tau^2 - 1)(u + 2\tau^2)}{\tau \sqrt{\tau^2 + u}} L(\sqrt{u}) + \frac{\pi(\sqrt{\tau^2 + u} - \tau)^2}{\sqrt{\tau^2 + u}} \\ &\quad \left. + \frac{(\tau^2 + 1)u}{u - 1} [1 - F(\sqrt{u})] \right]. \quad (\text{A.20}) \end{aligned}$$

Again, the NFW result appears in the infinite τ limit,

$$\psi''(u) = \frac{2GM_0}{c^2} \left[\frac{u + (2 - 3u)F(\sqrt{u})}{2u^2(u - 1)} - \frac{1}{u^2} \ln \left(\frac{\sqrt{u}}{2} \right) + O(\tau^{-2}) \right]. \quad (\text{A.21})$$

At this point, we can calculate the time delay, deflection angle, convergence, shear, and magnification of the truncated NFW lens. We will calculate one more derivative, deriving the so-called ‘‘flexion’’ (e.g., [45, 46]).

$$\psi'''(u) = \frac{2G}{c^2} \left[\frac{2M_{\text{proj}}(\sqrt{u})}{u^3} - \frac{2\pi r_s^2 \Sigma(\sqrt{u})}{u^2} + \frac{\pi r_s^2 \Sigma'(\sqrt{u})}{2u^{3/2}} \right] \quad (\text{A.22})$$

$$= -\frac{2\pi G r_s^2}{c^2 u^2} (u\Gamma' - \Gamma) \quad (\text{A.23})$$

$$\begin{aligned} &= \frac{2GM_0}{c^2} \frac{\tau^2}{2(\tau^2 + 1)^2 u^3} \left\{ \frac{3(\tau^2 + 1)^2 u}{2(\tau^2 + u)(u - 1)^2} [uF(\sqrt{u}) - 1] \right. \\ &\quad + \frac{u}{2(\tau^2 + u)(u - 1)} [(\tau^2 + 1 - 2(u - 1))uF(\sqrt{u}) \\ &\quad - (\tau^2 + 1)((u - 1) + 2\tau^2 + 3)] \\ &\quad + \frac{2(\tau^2 + 1)}{u - 1} [F(\sqrt{u}) - u] + 2 [2(u - 1) + 3\tau^2 + 1] F(\sqrt{u}) \\ &\quad + \frac{\tau^2 - 1}{2\tau(\tau^2 + u)^{3/2}} [3(3\tau^2 + u)(\tau^2 + u) - \tau^4] L(\sqrt{u}) \\ &\quad \left. + 4(\tau^2 - 1) \ln \tau - \frac{2\pi(\sqrt{\tau^2 + u} - \tau)^2}{\sqrt{\tau^2 + u}} + \frac{\pi u^2}{2(\tau^2 + u)^{3/2}} \right\}. \quad (\text{A.24}) \end{aligned}$$

Expanding about $\tau = \infty$, we find the NFW result,

$$\begin{aligned} \psi'''(u) &= \frac{2GM_0}{c^2} \left[\frac{(15u^2 - 20u + 8)F(\sqrt{u}) + 3u - 6u^2}{4u^3(u - 1)^2} \right. \\ &\quad \left. + 2 \ln \left(\frac{\sqrt{u}}{2} \right) + O(\tau^{-2}) \right]. \quad (\text{A.25}) \end{aligned}$$

For comparison, we institute a sharper cutoff,

$$\rho_T(x) = \frac{M_0}{4\pi r_s^3} \frac{1}{x(1+x)^2} \frac{\tau^4}{(\tau^2 + x^2)^2}. \quad (\text{A.26})$$

The total mass of this profile is

$$M = M_0 \frac{\tau^2}{2(\tau^2 + 1)^3} [2\tau^2(\tau^2 - 3) \ln \tau - (3\tau^2 - 1)(\tau^2 + 1 - \tau\pi)]. \quad (\text{A.27})$$

The projected mass density is

$$\begin{aligned} \Sigma(x) = \frac{M_0}{r_s^2} \frac{\tau^4}{4\pi(\tau^2 + 1)^3} & \left\{ \frac{2(\tau^2 + 1)}{x^2 - 1} [1 - F(x)] + 8F(x) \right. \\ & + \frac{\tau^4 - 1}{\tau^2(\tau^2 + x^2)} - \frac{\pi[4(\tau^2 + x^2) + \tau^2 + 1]}{(\tau^2 + x^2)^{3/2}} \\ & \left. + \frac{\tau^2(\tau^4 - 1) + (\tau^2 + x^2)(3\tau^4 - 6\tau^2 - 1)}{\tau^3(\tau^2 + x^2)^{3/2}} L(x) \right\}. \end{aligned} \quad (\text{A.28})$$

The total projected mass is obtained as before,

$$\begin{aligned} M_{\text{proj}}(x) = M_0 \frac{\tau^4}{2(\tau^2 + 1)^3} & \left\{ 2[\tau^2 + 1 + 4(x^2 - 1)]F(x) \right. \\ & + \frac{1}{\tau} [\pi(3\tau^2 - 1) + 2\tau(\tau^2 - 3) \ln \tau] \\ & + \frac{1}{\tau^3 \sqrt{\tau^2 + x^2}} [-\tau^3 \pi[4(\tau^2 + x^2) - \tau^2 - 1] \\ & \left. + [-\tau^2(\tau^4 - 1) + (\tau^2 + x^2)(3\tau^4 - 6\tau^2 - 1)] L(x)] \right\}. \end{aligned} \quad (\text{A.29})$$

Finally, the lensing potential is

$$\begin{aligned} \psi(u) = \frac{2GM_0}{c^2} \frac{1}{2(\tau^2 + 1)^3} & \left\{ 2\tau^3 \pi [(3\tau^2 - 1) \ln(\tau + \sqrt{\tau^2 + u}) \right. \\ & - 4\tau \sqrt{\tau^2 + u}] + 2(3\tau^4 - 6\tau^2 - 1)\tau \sqrt{\tau^2 + u} L(\sqrt{u}) \\ & + 2\tau^4(\tau^2 - 3) L^2(\sqrt{u}) + 16\tau^4(u - 1)F(\sqrt{u}) \\ & + 2\tau^4(\tau^2 - 3) \left(\cos^{-1} \frac{1}{\sqrt{u}} \right)^2 \\ & + \tau^2 [2\tau^2(\tau^2 - 3) \ln \tau - 3\tau^4 - 2\tau^2 + 1] \ln u \\ & + 2\tau^2 [\tau^2(4\tau\pi + (\tau^2 - 3) \ln^2 2 + 8 \ln 2) \\ & - \ln(2\tau)(1 + 6\tau^2 - 3\tau^4 + \tau^2(\tau^2 - 3) \ln(2\tau)) \\ & \left. - \tau\pi(3\tau^2 - 1) \ln(2\tau)] \right\}. \end{aligned} \quad (\text{A.30})$$

As before,

$$\psi'(u) = \frac{2G}{c^2} \frac{M_{\text{proj}}(\sqrt{u})}{u}. \quad (\text{A.31})$$

The second derivative follows,

$$\begin{aligned} \psi''(u) = \frac{2GM_0}{c^2} \frac{\tau^4}{4(\tau^2 + 1)^3 u^2} & \left\{ [-8(u - 1) + 2(1 - 3\tau^2)] F(\sqrt{u}) \right. \\ & - 4(\tau^2 - 3) \ln \tau + \frac{2(\tau^2 + 1)}{u - 1} [1 - F(\sqrt{u})] + 8 \\ & + \frac{(\tau^2 + u)(3\tau^4 - 6\tau^2 - 1) - \tau^2(\tau^4 - 1)}{\tau^2(\tau^2 + u)} \\ & \left. + \frac{2u(3\tau^4 - 6\tau^2 - 1)}{\tau^3(\tau^2 + u)^{1/2}} L(\sqrt{u}) \right\} \end{aligned}$$

$$\begin{aligned}
& - \frac{(3u + 2\tau^2)[(\tau^2 + u^2)(3\tau^4 - 6\tau^2 - 1) - \tau^2(\tau^4 - 1)]}{\tau^3(\tau^2 + u)^{3/2}} L(\sqrt{u}) \\
& - \frac{2\pi}{\tau}(3\tau^2 - 1) \\
& + \frac{\pi}{(\tau^2 + u)^{3/2}} \left[2(\tau^2 + u)(3\tau^2 - 1) + u(4(\tau^2 + u) - \tau^2 - 1) \right] \Big\} \quad (A.32)
\end{aligned}$$

Finally, the third derivative,

$$\begin{aligned}
\psi'''(u) = & \frac{2GM_0}{c^2} \frac{\tau^4}{8(\tau^2 + 1)^3 u^3} \left\{ \left[\frac{6(\tau^2 + 1)}{(u - 1)^2} + \frac{20\tau^2 + 12}{u - 1} + 30\tau^2 \right. \right. \\
& - 18 + 24(u - 1) \Big] F(\sqrt{u}) - \frac{1}{(\tau^2 + u)^2} \left[\frac{6(\tau^2 + 1)^3}{(u - 1)^2} \right. \\
& + \frac{2(\tau^2 + 1)^2(5\tau^2 + 7)}{u - 1} + 4(\tau^2 + 1)^2(u + \tau^2 + 2) \\
& + (2 + 3\tau^2)u^2 \Big] - \frac{8(\tau^2 + 1)}{u - 1} - 32 + 16(\tau^2 - 3) \ln \tau \\
& + \frac{u^2}{\tau^2(\tau^2 + u)^2} + \frac{8\pi}{\tau}(3\tau^2 - 1) \\
& - \frac{4[(\tau^2 + u)(3\tau^4 - 6\tau^2 - 1) - \tau^2(\tau^4 - 1)]}{\tau^2(\tau^2 + u)} \\
& - \frac{\pi [24\tau^6 + 3u^2(4u - 5) + 5\tau^2 u(9u - 4) + \tau^4(60u - 8)]}{(\tau^2 + u)^{5/2}} \\
& + \frac{16\tau^{10} + 30\tau^6 u(u - 4) + 9\tau^4 u^2(u - 10)}{\tau^3(\tau^2 + u)^{5/2}} L(\sqrt{u}) \\
& \left. + \frac{-3(6\tau^2 + 1)u^3 + 8\tau^8(5u - 6)}{\tau^3(\tau^2 + u)^{5/2}} L(\sqrt{u}) \right\} \quad (A.33)
\end{aligned}$$

All of these results reduce to the pure NFW case in the limit $\tau \rightarrow \infty$.

As a final comparison, we reproduce the [4] formulas for a sharp cutoff at $x = \tau$. In addition, we will derive the third derivative of the potential. First, we define the auxiliary function

$$T(x) = \frac{1}{\sqrt{x^2 - 1}} \left(\tan^{-1} \frac{\sqrt{\tau^2 - x^2}}{\sqrt{x^2 - 1}} - \tan^{-1} \frac{\sqrt{\tau^2 - x^2}}{\tau\sqrt{x^2 - 1}} \right), \quad (A.34)$$

choosing the branch where $T(x)$ is positive. This function is well defined everywhere provided we take the limit at $x = 1$, finding

$$T(1) = \sqrt{\frac{\tau - 1}{\tau + 1}} \quad (A.35)$$

Here, `ArcTan` from Mathematica and `catan` from C99 agree on the branch of $\tan^{-1}(x)$ for purely imaginary argument.

$$\Sigma(x) = \frac{M_0}{r_s^2} \frac{1}{2\pi} \left[\frac{1}{x^2 - 1} \left(\frac{\sqrt{\tau^2 - x^2}}{\tau + 1} - T(x) \right) \right]. \quad (A.36)$$

$$M_{\text{proj}}(x) = M_0 \left[\ln(1 + \tau) - \frac{\tau}{1 + \tau} + \frac{\sqrt{\tau^2 - x^2}}{\tau + 1} - \tanh^{-1} \frac{\sqrt{\tau^2 - x^2}}{\tau} + T(x) \right]. \quad (\text{A.37})$$

Note that the total mass is

$$M = M_{\text{proj}}(\tau) = M_0 \left[\ln(1 + \tau) - \frac{\tau}{1 + \tau} \right]. \quad (\text{A.38})$$

Note that these are valid only for $x \leq \tau$. For $x > \tau$, we simply have $\Sigma(x) = 0$ and $M_{\text{proj}}(x) = M$.

We find that the potential involves at least the polylogarithm Li_2 ; we do not find a simple expression. We start with the first derivative,

$$\psi'(u) = \frac{2G}{c^2} \frac{M_{\text{proj}}(\sqrt{u})}{u}. \quad (\text{A.39})$$

Assuming $u < \tau^2$,

$$\psi''(u) = -\frac{2GM_0}{c^2} \frac{1}{u^2} \left\{ \ln(1 + \tau) - \frac{\tau}{1 + \tau} + \frac{\sqrt{\tau^2 - u}}{\tau + 1} - \tanh^{-1} \frac{\sqrt{\tau^2 - u}}{\tau} - \frac{u\sqrt{\tau^2 - u}}{2(\tau + 1)(u - 1)} + \frac{3u - 2}{2(u - 1)} T(\sqrt{u}) \right\} \quad (\text{A.40})$$

$$\begin{aligned} \psi'''(u) = \frac{2GM_0}{c^2} \frac{2}{u^3} \left\{ \ln(1 + \tau) - \frac{\tau}{1 + \tau} + \frac{\sqrt{\tau^2 - u}}{\tau + 1} - \tanh^{-1} \frac{\sqrt{\tau^2 - u}}{\tau} - \frac{u\sqrt{\tau^2 - u}}{2(\tau + 1)(u - 1)} \right. \\ \left. + \frac{15u^2 - 20u + 8}{8(u - 1)^2} T(\sqrt{u}) + \frac{u[(u - 1)\tau + u(2 + u) - \tau^2(1 + 2u)]}{8(1 + \tau)\sqrt{\tau^2 - u}(u - 1)^2} \right\}. \quad (\text{A.41}) \end{aligned}$$

Note that as $u \rightarrow \tau^2$, ψ''' diverges (see also Figure 3). This is clearly because the surface mass density of this model is not smooth at $u = \tau^2$. On the other hand, for $u > \tau^2$, the derivatives can easily be computed as $\psi'(u) = 2GM/c^2u$, $\psi''(u) = -2GM/c^2u^2$, and $\psi'''(u) = 4GM/c^2u^3$.

Appendix B. The Sersic Profile

The Sersic profile describes the light distribution of elliptical galaxies, and it also can be made to fit the mass distribution of haloes [33]. This profile is defined in projection,

$$\Sigma(x) = \frac{M_0}{r_0^2 \pi (2n)!} \exp(-x^{1/n}), \quad (\text{B.1})$$

where r_0 is a scale radius and $x = r/r_0$. The effective radius r_e which contains half of the projected mass (or light) can be determined numerically. For the de Vaucouleurs

profile with $n = 4$, $r_e = 3459.5r_0$. The three-dimensional density distribution can be obtained by Abel inversion,

$$\begin{aligned}\rho(x) &= -\frac{1}{\pi r_0} \int_x^\infty \frac{dx'}{\sqrt{x'^2 - x^2}} \frac{d\Sigma}{dx'} \\ &= -\frac{1}{\pi r_0} \int_0^{\pi/2} du \sec u \frac{d\Sigma}{dx'} (x' = x \sec u),\end{aligned}\quad (\text{B.2})$$

and we find in practice that the integral with finite range works well numerically. As before, we need the total projected mass inside radius x ,

$$M_{\text{proj}}(x) = M_0 \left(1 - \frac{\Gamma(2n, x^{1/n})}{\Gamma(2n)} \right).\quad (\text{B.3})$$

The total mass is

$$M = M_0.\quad (\text{B.4})$$

The lensing potential can be expressed as a generalized hypergeometric function [35],

$$\psi(u) = \frac{2GM_0}{c^2} \frac{u}{(2n)!} {}_2F_2(2n, 2n; 2n+1, 2n+1; -u^{1/2n}),\quad (\text{B.5})$$

where again $u = x^2$. When $2n$ takes integer values, these results can be expressed in simpler terms as follows,

$$\begin{aligned}\psi(u) &= \frac{2GM_0}{c^2} 2n \left[\ln u^{1/2n} + \gamma - \text{Ei}(-u^{1/2n}) - a_0^n \right. \\ &\quad \left. + \exp(-u^{1/2n}) \sum_{j=0}^{2n-2} a_j^n \frac{u^{j/2n}}{j!} \right],\end{aligned}\quad (\text{B.6})$$

with

$$a_j^n = \sum_{k=j+1}^{2n-1} \frac{1}{k},\quad (\text{B.7})$$

and $\text{Ei}(x)$ being the exponential integral function. Now we calculate the derivatives of ψ . As before,

$$\psi'(u) = \frac{2G}{c^2} \frac{M_{\text{proj}}(\sqrt{u})}{u}.\quad (\text{B.8})$$

When $2n$ is an integer, we can express this in terms of elementary functions,

$$\psi'(u) = \frac{2GM_0}{c^2} \frac{1}{u} \left(1 - \exp(-u^{1/2n}) \sum_{j=0}^{2n-1} \frac{u^{j/2n}}{j!} \right).\quad (\text{B.9})$$

The second derivative is

$$\begin{aligned}\psi''(u) &= \frac{2GM_0}{c^2} \left[-\frac{1}{u^2} \left(1 - \exp(-u^{1/2n}) \sum_{j=0}^{2n-1} \frac{u^{j/2n}}{j!} \right) \right. \\ &\quad \left. + \frac{1}{u(2n)!} \exp(-u^{1/2n}) \right].\end{aligned}\quad (\text{B.10})$$

Finally, the third derivative is

$$\begin{aligned} \psi'''(u) = \frac{2GM_0}{c^2} \left[\frac{2}{u^3} \left(1 - \exp(-u^{1/2n}) \sum_{j=0}^{2n-1} \frac{u^{j/2n}}{j!} \right) \right. \\ \left. - \frac{1}{u^2(2n)!} \exp(-u^{1/2n}) \left(2 + \frac{u^{1/2n}}{2n} \right) \right]. \end{aligned} \quad (\text{B.11})$$

Appendix C. Elliptical Potentials

The power of considering ψ as a function of $u = x^2$ and not x becomes apparent when considering elliptical potentials. We will describe how the various observable quantities are obtained from the potential, and how these are modified for the case of an elliptical potential.

The deflection angle is just the gradient of the potential,

$$\vec{\alpha} = \vec{\nabla}\psi(u) = \psi'(u)\vec{\nabla}u. \quad (\text{C.1})$$

The lens equation is given by

$$\vec{s} = \vec{r} - \vec{\alpha}(\vec{r}), \quad (\text{C.2})$$

and thus the magnification matrix is

$$\mathbf{J} = \mathbf{I} - \vec{\nabla} \otimes \vec{\nabla}\psi(u). \quad (\text{C.3})$$

For this we need the second derivatives of ψ ,

$$\vec{\nabla} \otimes \vec{\nabla}\psi(u) = \psi'(u)\vec{\nabla} \otimes \vec{\nabla}u + \psi''(u)\vec{\nabla}u \otimes \vec{\nabla}u. \quad (\text{C.4})$$

Now we can define u so that the isopotential lines are ellipses and not circles:

$$u = (1 - \epsilon)x^2 + (1 + \epsilon)y^2, \quad (\text{C.5})$$

$$v = -(1 - \epsilon)x^2 + (1 + \epsilon)y^2, \quad (\text{C.6})$$

$$\vec{\nabla}u = \begin{pmatrix} 2(1 - \epsilon)x \\ 2(1 + \epsilon)y \end{pmatrix}, \quad (\text{C.7})$$

$$\vec{\nabla} \otimes \vec{\nabla}u = \begin{pmatrix} 2(1 - \epsilon) & 0 \\ 0 & 2(1 + \epsilon) \end{pmatrix}, \quad (\text{C.8})$$

and higher derivatives, such as the third needed for flexion, vanish. Deviations from ellipticity manifest as dependence on the variable v .

It is well known that elliptical isopotentials can lead to unphysical projected mass densities. For the singular isothermal sphere, $\epsilon > 0.2$ gives isodensity contours that become peanut-shaped. We propose a simple resolution to this problem that will be adequate for most purposes: add several elliptical potentials at the same location. We find that three potentials, one with ellipticity ϵ , one with ellipticity $f\epsilon$, and one circular potential, can be summed in such a way as to give nearly elliptical isodensity contours with ellipticities as large as $\epsilon = 0.8$, in other words axis ratios as large as three to one.

Consider a power-law density profile $\rho(r) \propto r^{-\gamma}$, yielding a potential $\psi(u) \propto u^{(3-\gamma)/2}$. We combine three such potentials,

$$\psi(u, v) = a_\epsilon \psi_\epsilon(u) + a_{f\epsilon} \psi_{f\epsilon}(u) + a_0 \psi_0(u), \quad (\text{C.9})$$

where the subscript indicates the ellipticity. Note that all three have purely elliptical isopotentials, but ellipses of one ellipticity are expressed with both the u and v variables of a different ellipticity. Expanding in ϵ , the v dependence can be canceled up through order ϵ^2 with the following choice of coefficients,

$$a_{f\epsilon} = \frac{2a_\epsilon}{f[(5-\gamma) - f(7-\gamma)]}, \quad (\text{C.10})$$

$$a_0 = (1-f) \left(\frac{7-\gamma}{3-\gamma} f - 1 \right) a_{f\epsilon}. \quad (\text{C.11})$$

A fraction $f = 1/2$ produces the best results in most cases,

$$a_{\epsilon/2} = \frac{8}{3-\gamma} a_\epsilon, \quad (\text{C.12})$$

$$a_0 = \frac{1+\gamma}{4(3-\gamma)} a_{\epsilon/2} = \frac{2(1+\gamma)}{(3-\gamma)^2} a_\epsilon. \quad (\text{C.13})$$

For potentials more complex than a pure power law, the cancellation is only exact at a single radius and hence the construction of the elliptical model which fits the wide range in radii is not trivial. We leave this issue for future work.

It is also well known that elliptical isopotentials can lead to an inferred surface mass density that is negative. This occurs for any finite ellipticity when the asymptotic density profile is r^{-3} or steeper. The total inferred mass is always positive however, and the negative surface mass densities inferred are small enough to not be a serious concern.

We make a note of the total mass of elliptical profiles here. Assume a profile described by a lensing potential $\psi(u)$ with u defined as above. In general, the surface density (inferred from the convergence) is given by

$$\Sigma \propto \psi' + \psi''(u + \epsilon v). \quad (\text{C.14})$$

If this inferred surface density contains a finite total mass, the total mass of the lens as a function of the ellipticity of the isopotentials is given by

$$M_{\text{tot}}(\epsilon) = \frac{1}{\sqrt{1-\epsilon^2}} M_{\text{tot}}(\epsilon = 0). \quad (\text{C.15})$$

More practically, we relate the following projected elliptical power-law mass density

$$\Sigma = \frac{3-\gamma}{2} [(1-\epsilon_{\text{iso}})x^2 + (1+\epsilon_{\text{iso}})y^2]^{(1-\gamma)/2}, \quad (\text{C.16})$$

with that derived by combining three elliptical isopotentials

$$\psi = b_\epsilon [a_\epsilon \psi_\epsilon + a_{\epsilon/2} \psi_{\epsilon/2} + a_0 \psi_0], \quad (\text{C.17})$$

where

$$\psi_\epsilon = \frac{[(1-\epsilon)x^2 + (1+\epsilon)y^2]^{(3-\gamma)/2}}{3-\gamma}. \quad (\text{C.18})$$

We find that the following fitting forms connect these two models in the range $1.2 \lesssim \gamma \lesssim 2.9$:

$$\epsilon = \epsilon_{\text{iso}} + [0.05(2.1 - \gamma)^2 + 0.257]\epsilon_{\text{iso}}^{0.4(1.8-\gamma)^2+2.9}, \quad (\text{C.19})$$

$$b_\epsilon = 1 + 0.193(-0.9 + \gamma)^{1.38}\epsilon_{\text{iso}}^2 + 0.0121(0.1 + \gamma)^{4.06}\epsilon_{\text{iso}}^6. \quad (\text{C.20})$$

This relation breaks down rapidly for $\epsilon_{\text{iso}} > 0.8$, corresponding to an axis ratio of 3:1. Two isodensity contours match with $\lesssim 0.6\%$ level at $\epsilon_{\text{iso}} < 0.6$ and $\lesssim 3\%$ level at $\epsilon_{\text{iso}} < 0.8$.